Article

Mechanical shutdown of battery separators: Silicon anode failure

Ji-Young Seo[1,5], Suhwan Kim [2,5], Jung-Hui Kim [1,5], Yong-Hyeok Lee[3], Jin-Young Shin[3], Somi Jeong[3], Dong-Wook Sung[3], Yong Min Lee [1,2] ✉ & Sang-Young Lee [1,4] ✉

The pulverization of silicon (Si) anode materials is recognized as a major cause of their poor cycling performance, yet a mechanistic understanding of this degradation from a full cell perspective remains elusive. Here, we identify an overlooked contributor to Si anode failure: mechanical shutdown of separators. Through mechano-structural characterization of Si full cells, combined with digital-twin simulation, we demonstrate that the volume expansion of Si exerts localized compressive stress on commercial polyethylene separators, leading to pore collapse. This structural disruption impairs ion transport across the separator, exacerbating redox nonuniformity and Si pulverization. Compression simulation reveals that a Young's modulus greater than 1 GPa is required for separators to withstand the volume expansion of Si. To fulfill this requirement, we design a high modulus separator, enabling a high-areal-capacity pouch-type Si full cell to retain 88% capacity after 400 cycles at a fast charge rate of 4.5 mA cm^{-2}.

Si, with its high theoretical specific capacity of 3592 mAh g^{-1}, outperforms graphite, the currently prevalent anode material of lithium (Li)-ion batteries, promising a substantial leap in cell energy densities and the resulting range and efficiency of electric vehicles and the capacity of portable electronics[1–3]. This potential of Si has catalyzed a surge in research and development efforts aimed at overcoming the intrinsic challenges hindering the utilization of its full capabilities in practical battery applications.

The main challenge to the use of Si as a mainstream anode material lies in its considerable volume expansion−up to 300%−during lithiation[4]. This expansion and the subsequent contraction during delithiation exert immense mechanical stress on the Si particles, leading to pulverization and loss of electrical connectivity in the Si anode. Moreover, this unwanted volume change destabilizes the solid electrolyte interphase (SEI) layers formed on Si. The repeated breaking and reforming of the SEI layers continuously consume electrolytes, further degrading cycling performance[5–7].

Enormous efforts, including the nanostructuring of Si to accommodate the volume change of Si and mitigate pulverization[8–10], electrolyte synthesis and formulation for SEI stabilization[11,12], and the design of anode binders that maintain electrode integrity despite volume fluctuations[13–15], have been devoted to address this issue. Despite these advances, the quest for durable, high-capacity Si anodes remains a vibrant area of research. The complexity of the interactions between Si, electrolytes, and binders, coupled with the stringent requirements for practical battery applications, necessitates ongoing innovation. Particularly, the volume expansion of Si, coupled with its intricate electrochemical behavior, has prompted an investigation into its electrochemical interplay with other components in full cells, an aspect overlooked in previous studies. Therefore, a thorough understanding of the underlying failure mechanism of Si anodes from a full cell perspective is imperative to achieve prolonged cycle life.

Here, we report on the mechanical shutdown phenomena that occur in battery separators, serving as a hidden culprit in the cycling

[1]Department of Chemical and Biomolecular Engineering, Yonsei University, Seoul, Republic of Korea. [2]Department of Energy Science & Engineering, Daegu Gyeongbuk Institute of Science and Technology, Daegu, Republic of Korea. [3]R&D Campus Daejeon, LG Energy Solution, Daejeon, Republic of Korea. [4]Department of Battery Engineering, Yonsei University, Seoul, Republic of Korea. [5]These authors contributed equally: Ji-Young Seo, Suhwan Kim, Jung-Hui Kim. ✉e-mail: yongmin@yonsei.ac.kr; syleek@yonsei.ac.kr

degradation of Si full cells. By assessing the resistances of individual cell components during cycling, we observed a notable increase in bulk ionic resistance, prompting further investigation into the structural integrity of battery separators in terms of their pore disruption. Through the mechano-structural analysis of Si full cells, combined with digital-twin simulation, we observed that localized compressive stress induced by the volumetric expansion of micro-sized Si subjects the separator to pressure, resulting in the collapse of the separator pores—a phenomenon termed mechanical shutdown. Quantitative characterization of the pore structure changes during cycling was performed using scanning electrochemical microscopy (SECM) analysis, revealing that this mechanical shutdown impeded ion transport across the separator, thereby exacerbating redox inhomogeneity and Si pulverization.

Mechanical compression simulations demonstrated that a battery separator with Young's modulus exceeding 1 GPa is needed to stably maintain its porous structure when paired with micro-sized Si anodes. To meet this requirement, we designed a high modulus (HM) separator with a Young's modulus of above 1 GPa. The HM separator was assembled with a pure Si anode (areal capacity of 8.5 mAh cm^{-2}) and a LiNi$_{1-x-y-z}$Co$_x$Mn$_y$Al$_z$O$_2$ (NCMA) cathode (areal capacity of 4.5 mAh cm^{-2}) to fabricate a high-areal-capacity pouch-type full cell. Driven by its structural robustness, the HM separator enabled stable cyclability in the full cell, which retained 88% of its capacity after 400 cycles at a fast charge rate of 4.5 mA cm^{-2}, far exceeding those of previously reported Si full cells. This study offers an insight into the design of separators aimed at prolonging the lifespan of Si full cells.

Results

Unveiling the separator degradation during the cycling of Si full cells

To clarify the issue with the cyclability of Si anodes, pouch-type full cells comprising of an NCMA cathode (4.5 mAh cm^{-2}) and different anodes (micro-sized Si anode (8.5 mAh cm^{-2}) vs. graphite anode (5.0 mAh cm^{-2})) were fabricated. To ensure intimate interfacial contact between the cell components during cycling, a stack pressure of 100 kPa was applied to the full cells. Meanwhile, in the absence of this stack pressure, the Si full cell demonstrated a rapid decline in its capacity retention and fluctuating voltage profiles (Supplementary Fig. 1), which can be attributed to the volume expansion of the micro-sized Si anode with cycling[16] (Supplementary Fig. 2).

We observed that the capacity retention of the Si full cell, which was 59% after 400 cycles, was significantly lower than that (89%) of the graphite full cell (Fig. 1a and Supplementary Fig. 3). To identify the underlying failure mechanism of the Si full cell, electrochemical impedance spectroscopy (EIS) analysis was conducted at different cycle numbers (Supplementary Fig. 4). There was an increase in the charge transfer resistance (R_{ct}) and solid-electrolyte interphase (SEI) resistance (R_{SEI}) of the Si full cells after cycling, indicating the thickening of passivation layers and loss of electrical contact, which are known as major causes of cycling failure in Si full cells[17]. A notable finding was the substantial increase in the bulk resistance (R_{bulk}) of the Si full cell (= 99%) compared to that of the graphite full cell (= 4%) (Fig. 1b).
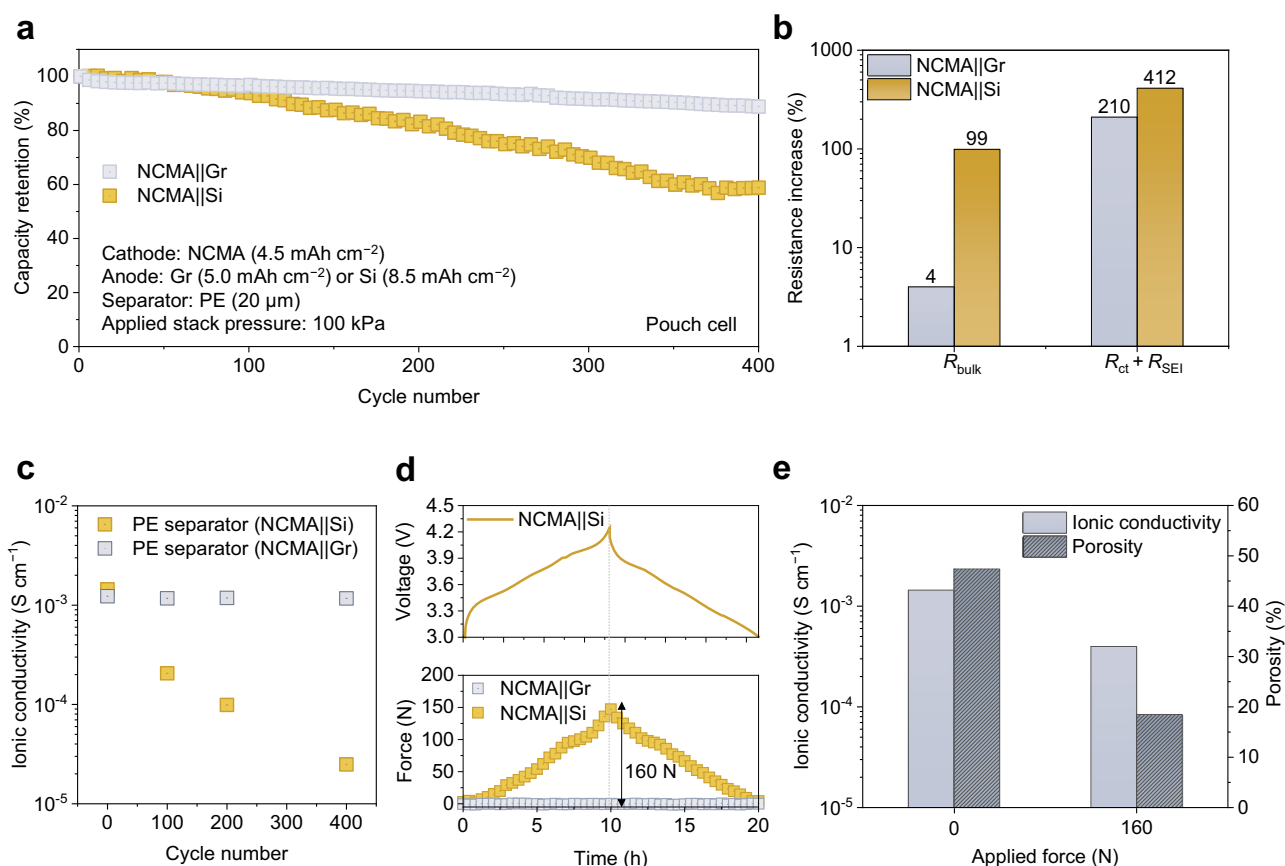

Fig. 1 | Separator degradation during the cycling of the Si full cells. a Cycling performance of the full cells with different anodes: NCMA cathode (4.5 mAh cm^{-2})/ graphite anode (5.0 mAh cm^{-2}) or pure micro-sized Si anode (8.5 mAh cm^{-2}). **b** Change in the R_b and ($R_{ct} + R_{SEI}$) of the full cells (graphite vs. Si) before and after 400 cycles. **c** Change in the ionic conductivity of the polyethylene (PE) separators as a function of the cycle number (graphite vs. Si). **d** Internal force evolution with time during charging/discharging (graphite vs. Si). **e** Change in ionic conductivity and porosity of PE separators before and after the mechanical compression with a stack force of 160 N during the model study.

To elucidate this behavior, the R_{bulk} was deconvoluted using the Eq. (1)[18,19]:

$$R_{bulk} = R_{NCMA} + R_{Si} + R_{electrolyte-sep} + R_{tab} \qquad (1)$$

Under the assumption that the tab resistance (R_{tab}) remained constant, we measured the electronic resistance of the Si anode (R_{Si}) and NCMA cathode (R_{NCMA}) after disassembling the cell (Supplementary Fig. 4). We observed that the increase in the R_{bulk} of the Si full cell was strongly influenced by an increase in the $R_{electrolyte-sep}$. This result was verified by monitoring the change in ionic conductivity of the cycled polyethylene (PE) separators as a function of the cycle number (Supplementary Fig. 5). The ionic conductivity of the cycled PE separator in the Si full cell decreased sharply from 1.2×10^{-3} to 2.5×10^{-5} S cm^{-1} after 400 cycles, whereas that of the PE separator in the graphite full cell remained almost unchanged (Fig. 1c). Prior to measuring ionic conductivity, the separators retrieved from the cycled cells were washed several times to ensure removal of residual contaminants (Supplementary Fig. 6). To address concerns on the residual Si particles, we analyzed the surface of the cycled separators (after 100th cycle). Negligible amounts of Si particles were detected on the surface of the separators. During the ionic conductivity measurement, no additional stack pressure was applied to the cycled separators. Next, an operando measurement of the internal force evolution of the Si full cells during repeated lithiation/delithiation was performed using a load cell apparatus under the externally applied stack pressure of 100 kPa (Supplementary Fig. 7). The internal force refers to the force newly generated by the volume expansion of Si during the lithiation in the Si full cells. The internal force of the Si full cells tended to increase during lithiation, reaching a peak force of 160 N, and this behavior was consistent with the voltage profile (Fig. 1d), indicating the generation of electromechanical stress induced by the lithiation of the Si anode.

To further understand the effect of the newly evolved electromechanical stress on the ionic conductivity of the PE separator, a model study was conducted. To this end, a pristine PE separator was subjected to mechanical compression under a stack force of 160 N, corresponding to the peak force observed in the previously described operando measurement. The ionic conductivity of the compressed PE separator reduced from an initial value of 1.44 to 0.4 mS cm^{-1}, and this was accompanied by a decrease in the porosity (from 47.8 to 18.5%) and surface area (from 118.0 to 31.8 m^2 g^{-1}) of the PE separator (Fig. 1e and Supplementary Fig. 8). These results demonstrate that the internal stress induced by the volume expansion of the lithiated Si resulted in the structural disruption of the PE separator, thereby impeding ion transport.

Digital-twin simulation of the separator pore collapse upon Si volume expansion

The mechanical deformation behavior of the PE separator in the Si full cell was analyzed using 3D digital-twin cell modeling and simulations. A virtual 3D model of the PE separator structure (Fig. 2a) was constructed by incorporating the relevant structural parameters (Supplementary Figs. 9, 10) and basic mechanical properties (Supplementary Table 1). Subsequently, the structural deformation behavior of the PE separator upon exposure to the volumetric expansion of Si was theoretically investigated using a compressive force of 160 N, corresponding to the internal force evolved during charging/discharging of the Si full cells under the externally applied stack pressure of 100 kPa (shown in Fig. 1d). The pressure applied to the PE separator during the simulation was calculated to be 6.03 MPa, whereas the apparent pressure (without the compressive force) was 0.4 MPa (Supplementary Fig. 11).

This discrepancy between the simulated and apparent pressures prompted us to conduct a theoretical analysis of the intersection (denoted as effective contact area) between the PE separator and electrode active particles (Fig. 2b and Supplementary Table 2). We observed that a polymeric region accounted for 50.6% of the total area of the PE separator (PE, gray bar in Fig. 2c, top), and this fraction reduced to 17.7% upon the contact of the PE separator with Si particles (PE-Si, yellow bar in Fig. 2c, middle). This value further decreased to 6.3% when the PE separator was in contact with both Si and NCMA particles (PE-Si-NCMA, red bar in Fig. 2c, bottom). Such a reduction in the effective contact area of the PE separator led to the concentration of the stack pressure. Consequently, the local compressive pressure exerted on the PE separator under the compressive force of 160 N was calculated to be 6 MPa, which was significantly higher than the externally applied stack pressure of 100 kPa.

The 3D digital-twin structural model revealed that the pores of the PE separator in the Si full cells experienced mechanical rupture when subjected to a pressure of 6 MPa, and this rupture was particularly pronounced at the interface of the separator−Si particles (red-dashed lines in Fig. 2d, e). In contrast, the PE separator in contact with the electrode pores remained unaffected (blue-dashed line in Fig. 2d, e). This result indicates the concentration of the internal force induced by the volume expansion of Si at the interface of the separator−electrode particles, leading to the local collapse of the separator pores. This finding was experimentally verified through a model study (Supplementary Fig. 12). During the model study, the PE separator positioned between the Si anode and NCMA cathode was observed to become translucent when subjected to an apparent stack force of 160 N, indicating the collapse of the pores owing to the local compressive pressure exerted by the Si and NCMA particles. In contrast, a PE separator placed between metallic current collectors remained almost unchanged at the same stack force.

Based on the understanding of the effective contact area described above, we conducted simulations to explore the effect of the local compressive pressure on the pore structure and ion transport of the PE separator in Si full cells. In a pristine state (local compressive pressure = 0 MPa), the PE separator exhibited uniform ion channels with high Li$^+$ density owing to its well-developed pore structure (Fig. 2f). Meanwhile, in the absence of the externally applied stack pressure, the pore structure and ionic conductivity of the cycled PE separator in both Si full cells and graphite full cells remained almost unchanged, indicating that the structural deformation of the PE separator is not observed despite the volume expansion of Si during cell cycling (Supplementary Figs. 13, 14). In contrast, when the PE separator was subjected to local compressive pressure, its pore structure collapsed, resulting in a reduction in the Li$^+$ density. Consequently, the ionic conductivity decreased by 82% (from 0.92 to 0.17 mS cm^{-1}; Fig. 2g), and the porosity decreased by 70% (from 47.3 to 14.2%; Fig. 2h), which is consistent with the experimental results.

Spatio-temporal electrochemical analysis of the pore collapse of separators during the cycling of Si full cells

Driven by the previously described results, we monitored the variation in the Li$^+$ transport phenomena across the separator during cycling, which is crucial for elucidating the capacity degradation of Si full cells. It is noteworthy that conventional structural analysis methods, such as atomic force microscopy (AFM) or scanning electron microscopy (SEM), have limitations in identifying the spatial evolution of Li$^+$ migration in the pore channels of the PE separator. To address this issue, we designed an analytical approach based on scanning electrochemical microscopy (SECM) using a Pt microprobe and redox mediator (ferrocene, Fc; details in Supplementary Fig. 15 and Supplementary Note 1). We observed the diffusion of an oxidized molecule (ferrocenium, Fc$^+$) generated at the Au electrode through the separator, after which the current required to reduce Fc$^+$ was measured at the microprobe to quantitatively characterize the spatial evolution of ion migration (Fig. 3a).
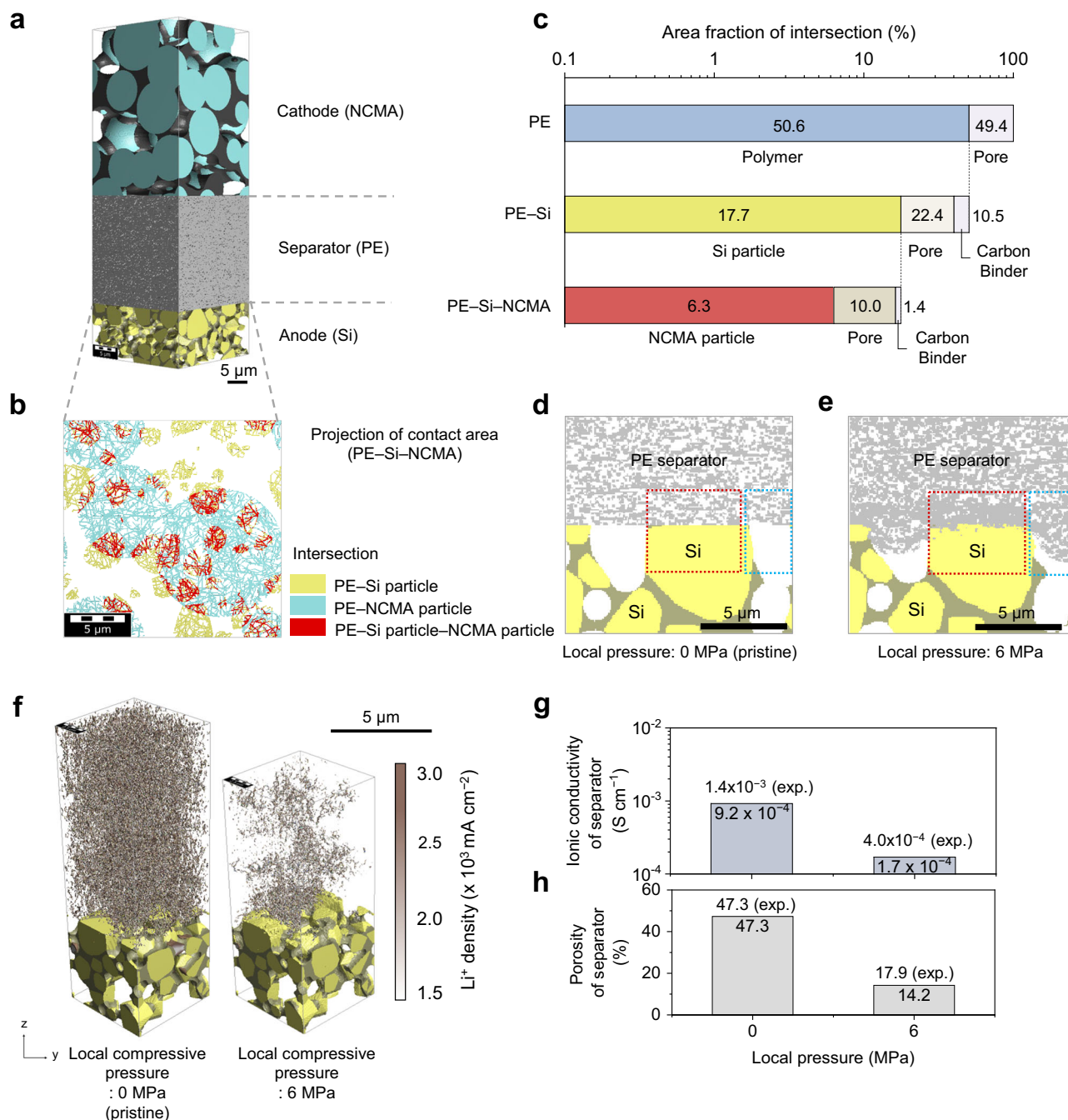
Fig. 2 | Digital-twin simulation of the separator pore collapse upon Si volume expansion. a A digital-twin 3D model structure of the Si full cell. **b** Theoretical projection of the intersection (effective contact area) between the PE separator and electrode active particles. **c** A chart showing the area fraction of the intersection between the PE separator and electrode active particles: The first row represents the area fraction occupied by the polymeric region and pore in the PE separator; the second row represents the area fraction of the anode constituents in contact with the polymeric region of the PE separator; and the third row represents the fraction of the cathode constituents in contact with the polymeric region of the PE separator and Si active particles (Source data are provided as a Source Data file). **d**, **e** Simulated pore structure of the interface of PE separator–Si anode under a pressure of 0 MPa (**d**), and 6 MPa (**e**). **f** Variations in the Li⁺ density distribution in the PE separator before and after exposure to the local compressive pressure. **g**, **h** Ion conductivity (**g**) and porosity (**h**) of the PE separator before and after exposure to the local pressure (Source data of Fig. 2f–h are provided as a Source Data file).

A pristine PE separator (before the cycle test) exhibited a consistent and high average current (~148 pA) over the entire area, indicating a uniform ion transport throughout the separator (left, Fig. 3b). However, the cycled PE separator (after 100 cycles) exhibited reduced currents with an uneven distribution (middle, Fig. 3b), revealing the formation of locally collapsed pores. Consequently, ionic flow was not permitted through the collapsed pores but was diverted to adjacent open pores. Such spatial inhomogeneity in ion transport is expected to

concentrate the redox reactions of Si anodes near open pores[20,21], thus exacerbating the volume expansion of Si anodes and further disrupting the remaining open pores. Eventually, the cycled PE separator (after 400 cycles) exhibited a considerably reduced average current (~11 pA) owing to the prevalence of collapsed pores (right, Fig. 3b).

This spatio-temporal electrochemical analysis of the separators was corroborated by monitoring the change in their surface morphologies and ionic conductivities during cycling. The pristine PE
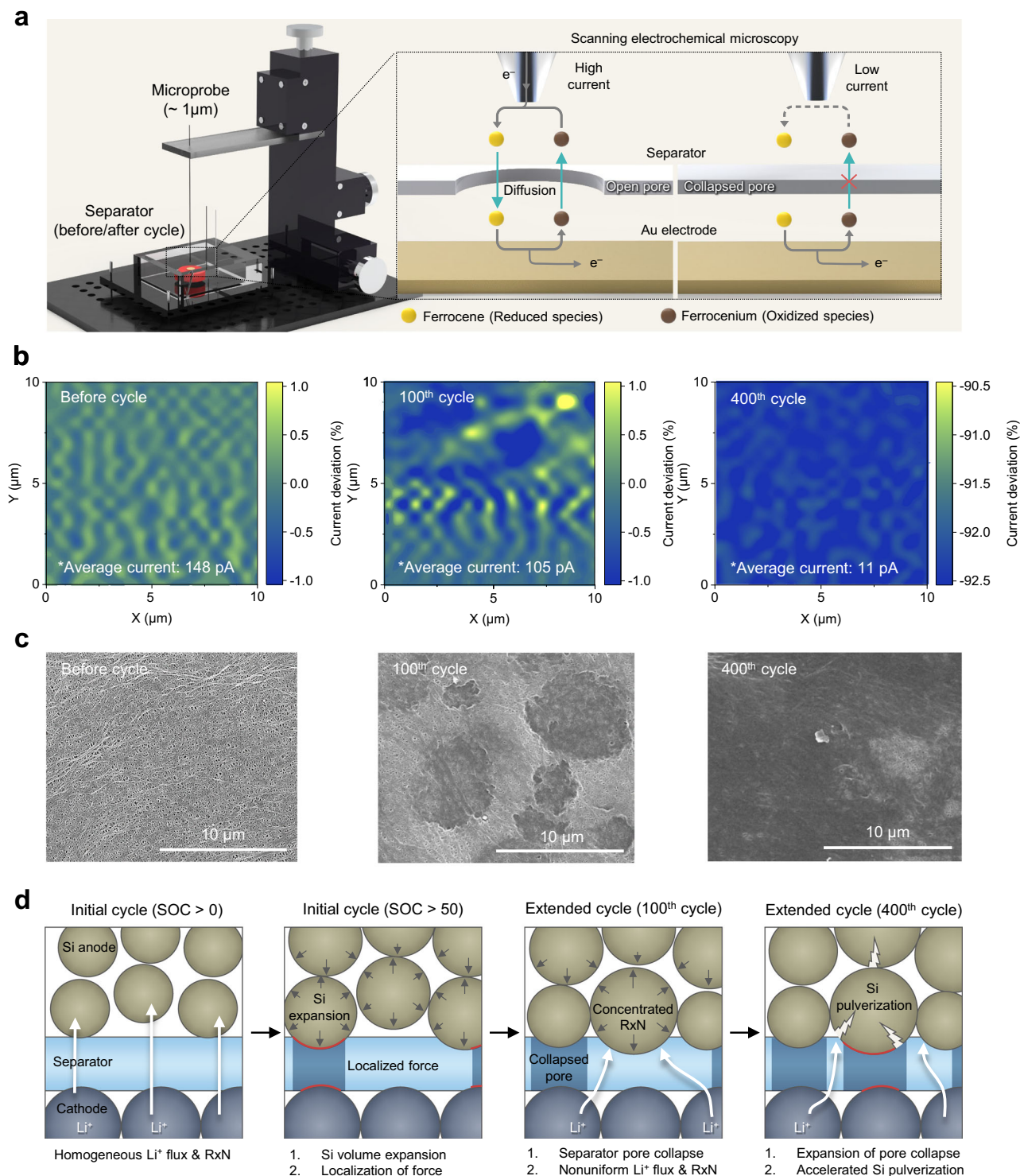
Fig. 3 | Spatio-temporal electrochemical analysis of the pore collapse of the separators during cycling of the Si full cells. a Schematic illustration of scanning electrochemical microscopy (SECM) analysis for identifying ion transport phenomena through separators. **b** SECM images of PE separators before cycling (left), after 100 cycles (middle), and after 400 cycles (right). **c** Corresponding scanning electron microscopy (SEM) images of the PE separators before cycling (left), after 100 cycles (middle), and after 400 cycles (right), in which the PE separators were obtained from the pouch-type Si full cells (NCMA cathode (4.5 mAh cm⁻²)||pure micro-sized Si anode (8.5 mAh cm⁻²)) as a function of cycle number. **d** Dynamic failure model of the separator in Si full cells during cycling: morphology evolution and degradation processes of the Si-based LIBs during cycling.

separator exhibited a well-developed and uniform pore structure (ionic conductivity = 1.44 mS cm⁻¹; left, Figs. 3c, 1c). The cycled PE separator (after 100 cycles) exhibited a partially disrupted pore structure (0.21 mS cm⁻¹; middle, Figs. 3c, 1c), which was almost collapsed (0.02 mS cm⁻¹) after 400 cycles (right, Figs. 3c, 1c). These results demonstrate that the local compressive pressure induced by the volume expansion of Si during cycling persistently disrupted the porous structure of the PE separator, suggesting a dynamic failure model of the PE separator, which degraded the electrochemical performance of the Si full cells (Fig. 3d).

Design of the HM separator customized for Si full cells

Next, we investigated the change in the porosity and strain of separators as a function of Young's modulus using mechanical compression simulations to replicate stress conditions ranging from 2.3 to 7.4 MPa. Young's modulus is a key indicator of the elasticity of a material, as it indicates the ability of the material to resist deformation under stress[22]. As the stack pressure applied to the separators increased, the change in the porosity (Supplementary Fig. 16a) and strain (Supplementary Fig. 16b) of the separators tended to become more pronounced. We observed that when Young's modulus of the separators was higher than 1.0 GPa, the change in the porosity and strain was negligible, even at the elevated stack pressure. Consequently, the change in the ionic conductivity of the separators with Young's modulus higher than 1.0 GPa was negligible even at a stack pressure of 6.0 MPa (Fig. 4a). As a complementary study, we theoretically investigated the structural stability of a model separator with Young's modulus of 1.0 GPa (Supplementary Fig. 17). Under the local compressive pressure of 6.0 MPa, the model separator exhibited inappreciable change in its porous structure and Li+ density distribution. To verify this theoretical understanding, we fabricated an Al$_2$O$_3$/PAN composite separator with a Young's modulus of approximately 1 GPa. This composite separator showed an insignificant difference in the ionic conductivity before and after being subjected to a compressive pressure of 6.0 MPa (Supplementary Fig. 18), indicating that the composite separator with Young's modulus of ~1 GPa can resist the structural collapse caused by the volume expansion of Si. This mechanical analysis offers a design guide for pressure-resistant separators tailored to Si full cells.

To experimentally validate the results obtained from the mechanical compression simulations, we fabricated an HM separator through the simultaneous electrospraying of Al$_2$O$_3$ particles and electrospinning of polyacrylonitrile (PAN) nanofibers (Supplementary Fig. 19). Thereafter, the separator was subjected to a roll pressing process to obtain a self-standing HM separator. A cross-sectional SEM image revealed that the HM separator was composed of densely-packed Al$_2$O$_3$ particles spatially besieged by the electrospun PAN nanofibers (Fig. 4b). In addition, thermogravimetric analysis (TGA) measurement revealed that the composition ratio of the HM separator was Al$_2$O$_3$/PAN = 93/7 (w/w) (Supplementary Fig. 20). The mercury porosimetry analysis revealed that the average pore size of the HM separator was approximately 520 nm (Supplementary Fig. 21), which is comparable to that of the PE separator.

Next, the average Young's modulus of the HM separator was estimated through nanoindentation analysis as 2.14 GPa, which was significantly higher than that of the PE separator (0.18 GPa; Fig. 4c). In order to highlight the high Young's modulus of the HM separator, control separators with different composition ratios of Al$_2$O$_3$/PAN (= 20/80 and 80/20 (w/w)) were prepared. These control separators showed Young's moduli of 0.12 and 1.15 GPa, respectively, which were significantly lower than that of the HM separator (2.14 GPa) (Supplementary Fig. 22). As described previously, the HM separator was produced by the simultaneous electrospraying of Al$_2$O$_3$ and electrospinning of PAN. This fabrication technique allowed the polymer to form independent nanofibers rather than encapsulating the inorganic particles, thereby leveraging the high Young's modulus of the inorganic particles with minimal polymer content to produce the porous, free-standing separator. This high Young's modulus of the HM separator exceeded the previously established benchmark of 1.0 GPa, making it a viable candidate separator that validates the credibility of the mechanical compression simulation. To demonstrate the advantageous effects of the HM separator in the Si full cells, a virtual 3D model of the HM separator structure was constructed using the same methodology used for the PE separator while considering the mass ratio, particle/fiber shape, and distribution (Supplementary Figs. 23, 24 and Supplementary Table 3). This mechanical compression simulation revealed that change in the pore structure and Li+ density of the HM separator was negligible even at the stack pressure of 6.0 MPa (Fig. 4d). Subsequently, we calculated the pressure required to induce the structural deformation of the HM separator, corresponding to the strain equivalent to pore collapse in the PE separator. A substantially higher pressure of 940 MPa was required for the structural collapse of the HM separator, which is over 150 times higher than that required for the PE separator (6.0 MPa; Supplementary Fig. 25).

This quantitative comparison of the mechano-structural properties of the HM and PE separators suggests that separators with a low Young's modulus are susceptible to structural collapse owing to the local compressive pressure generated by the volume expansion of Si, resulting in the disruption of ion channels. In contrast, a separator with a high Young's modulus above a critical threshold of 1.0 GPa can maintain its porous structure even when in contact with lithiated Si particles, thus allowing facile ion transport across the separator (Fig. 4e).

Achieving the stable cycling performance of high-areal-capacity Si full cells by the HM separator

The effect of the HM separator on the cycling performance of the high-areal-capacity Si full cell (NCMA cathode (4.5 mAh cm^{-2})||pure micro-sized Si anode (8.5 mAh cm^{-2}), N (negative electrode capacity)/P (positive electrode capacity) ratio = 1.89)) was investigated under practical operating conditions (charge/discharge current densities = 1.0 C (4.5 mA cm^{-2})/0.5 C (2.25 mA cm^{-2})). The cell assembled with the HM separator exhibited higher capacity retention (81% after 400 cycles) compared to the cell with the PE separator (59 %) (Fig. 5a and Supplementary Fig. 26). In addition, the cycling performance of the Si full cell was further examined at a low N/P ratio of 1.55 (NCMA cathode (4.5 mAh cm^{-2})|| pure micro-sized Si anode (7.0 mAh cm^{-2})). Similar to the result observed at the N/P ratio of 1.89, the cell with the HM separator still exhibited higher capacity retention (75% after 300 cycles) compared to the cell with the PE separator (59%) (Supplementary Fig. 27). This result was verified by monitoring the ionic conductivities of the cycled separators as a function of the cycle number. The HM separator stably maintained its ionic conductivity over the entire cycle numbers, whereas the ionic conductivity of the PE separator decreased gradually with an increase in the cycle number (Fig. 5b and Supplementary Fig. 28). Moreover, there was no notable change in the porous structure of the HM separator after 400 cycles (Supplementary Fig. 29), indicating its mechanical resistance to the internal stress generated in the Si full cell.

To address the concern regarding the heavy weight of the HM separator (areal density = 4.9 mg cm^{-2} vs. 1.5 mg cm^{-2} for PE separator), the specific energy densities of the cells were estimated (Supplementary Fig. 30 and Supplementary Table 4). A minor difference in the cell energy density was observed between the HM and PE separators, due to the relatively low mass fraction (7%) of the separator in the cell. Meanwhile, the improved capacity retention of the Si full cell with the HM separator resulted in a higher specific energy density (211 Wh kg$_{cell}^{-1}$) after 400 cycles compared to the cell with the PE separator (161 Wh kg$_{cell}^{-1}$). This comparison demonstrates the superior performance of the HM separator in maintaining the cell energy density over the extended cycle. This superior cyclability of the HM separator was further elucidated by analyzing the EIS spectra of the full cell (Supplementary Fig. 31). After 400 cycles, the full cell with the HM separator exhibited a suppressed increase in R_b and $R_{ct} + R_{SEI}$, which was a significant improvement compared to the results of the full cell with the PE separator (Fig. 5c). This result was confirmed by analyzing the cross-sectional SEM images of the cycled Si anodes. Compared to the PE separator, the HM separator enabled the cycled Si anode to retain its structural integrity (Fig. 5d). The HM separator, due to its structural robustness, is expected to maintain its porous structure during cycling, thereby facilitating stable and uniform ion migration
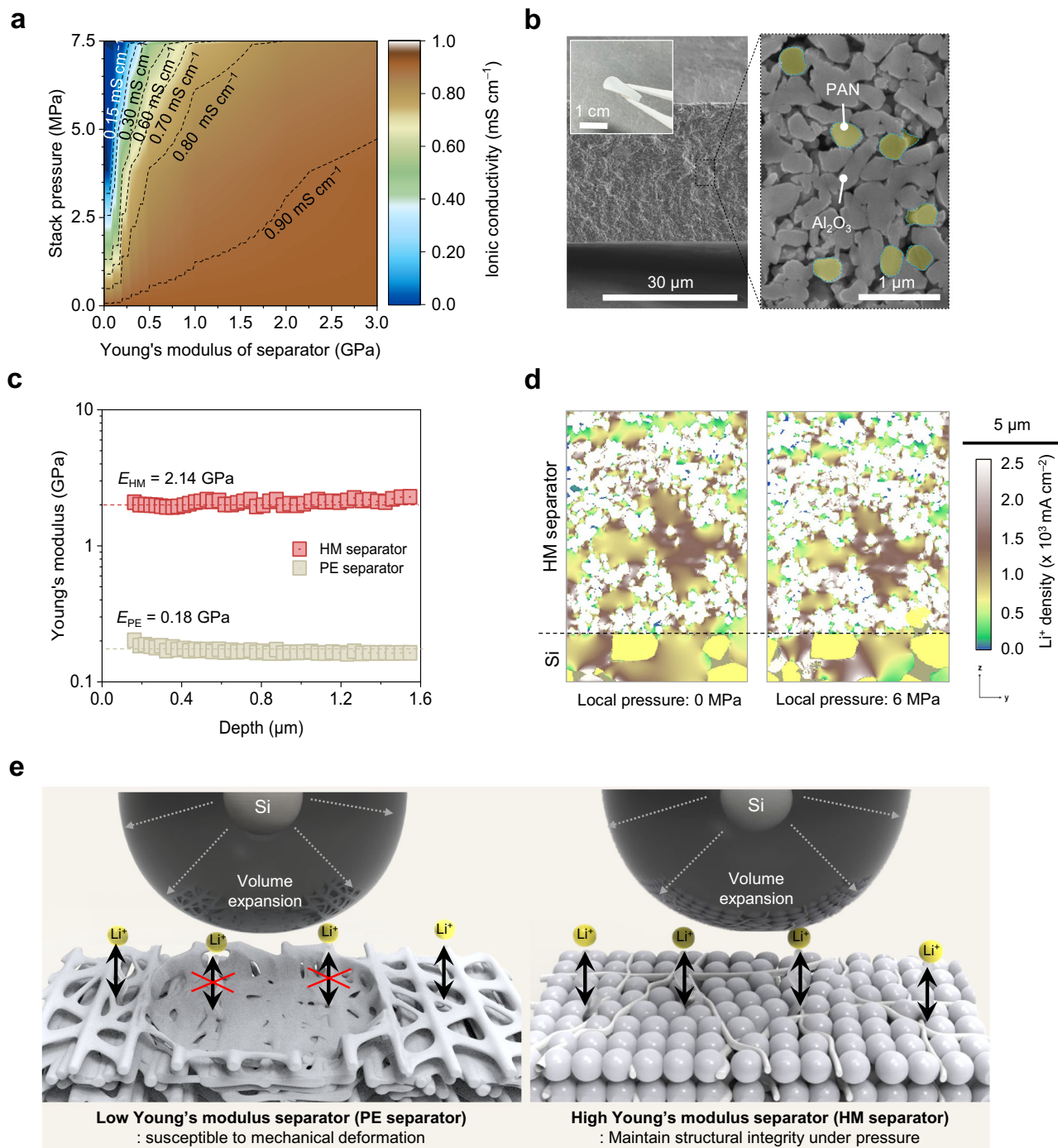
Fig. 4 | Design of the high modulus (HM) separator customized for Si anodes. **a** Calculated ionic conductivities of the separators under various applied stack pressures as a function of Young's modulus of the separators (Source data are provided as a Source Data file). **b** Cross-sectional SEM images of the HM separator, in which the inset shows its photograph. **c** Young's modulus of the PE separator (vs. HM separator) as a function of the indentation depth. **d** Variation in the Li$^+$ density distribution in the HM separator before and after exposure to a stack pressure of 6.0 MPa (Source data are provided as a Source Data file). **e** Schematic illustration depicting the change in the structure of the PE separator (vs. HM separator) upon contact with the lithiated Si particles undergoing severe volume expansion.

toward the Si anode. Consequently, the irregular and localized volume expansion of Si could be suppressed, mitigating the volume change of the cycled Si anode. These results demonstrate the advantageous contribution of the HM separator to the structural stability of the Si anode during cycling.

It is known that the application of an optimum external pressure to Si full cells can enhance their cycle life by suppressing the volume expansion of Si anodes[23,24]. Based on these previously reported results, we selected an externally applied stack pressure of 800 kPa,

representing a benchmark pressure above the stack pressure (= 100 kPa) of the cells examined in this study. Future research will focus on optimizing the externally applied stack pressure in Si full cells. The high-areal-capacity pouch-type Si full cells (NCMA cathode (4.5 mAh cm^{-2})||Si anode (8.5 mAh cm^{-2})) were subjected to an externally applied stack pressure of 800 kPa (Fig. 5e), which was higher than the typical stack pressure (= 100 kPa) of the aforementioned cells. Under this operating condition, the full cell with the HM separator demonstrated improved capacity retention (88% after 400 cycles)
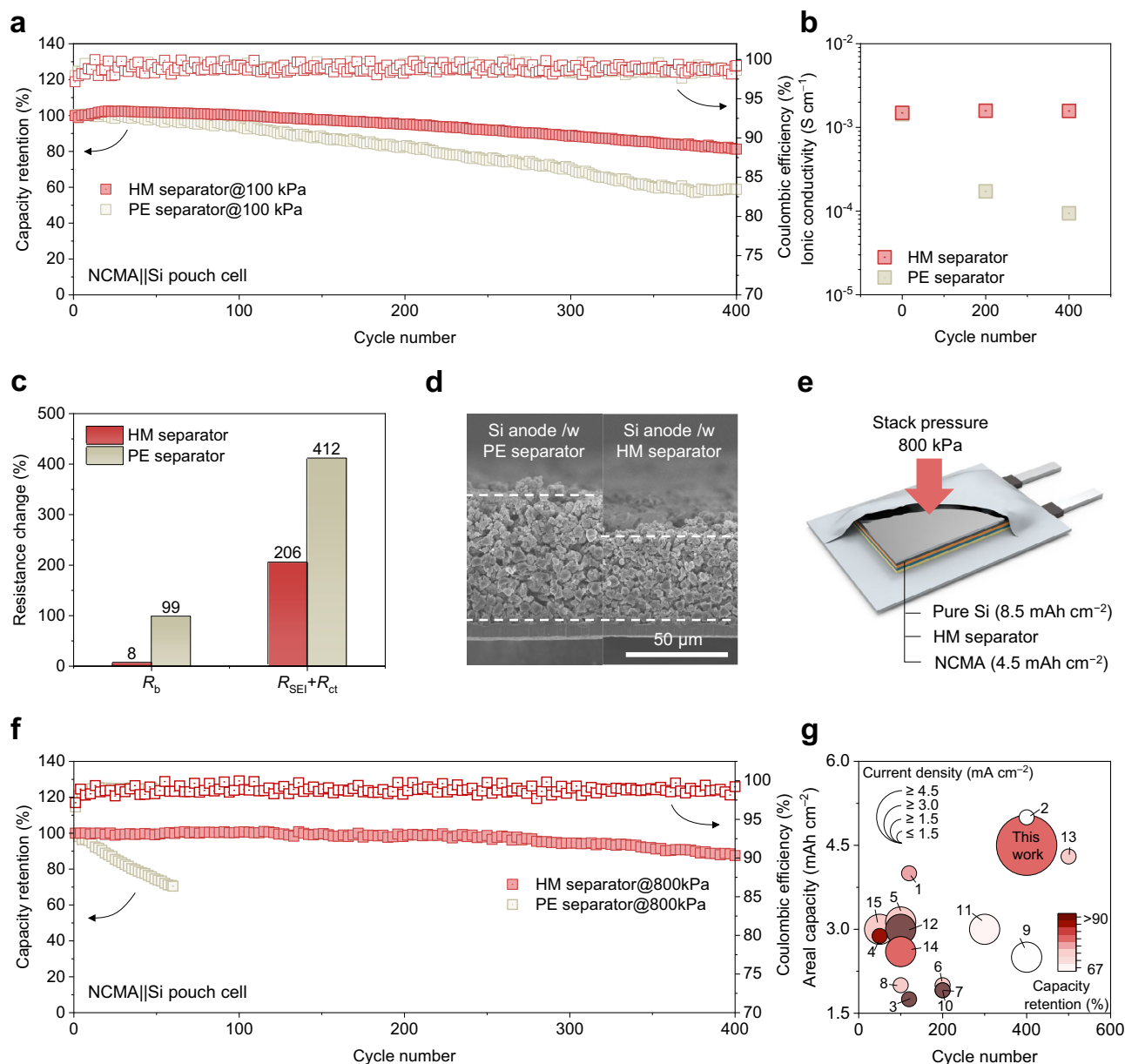
Fig. 5 | Cycling performance of Si full cells assembled with the HM separator.
a Cycling performance of Si full cells containing the NCMA cathode (NCMA:
4.5 mAh cm^{-2}, pure Si anode: 8.5 mAh cm^{-2}) at a charge/discharge current rate of
1.0 C/0.5 C and voltage range of 3.2 – 4.25 V under the externally applied stack
pressure of 100 kPa. **b** Changes in ionic conductivity as a function of cycle progress
of Si full cell containing different separators (HM separator vs. PE separator). **c** Plot
of R_b/R_{ct+SEI} of Si full cells containing the HM separator and PE separator after the
200th, and 400th cycle. **d** Cross-sectional SEM images of cycled Si anode with PE
separator (left side) and HM separator (right side). **e** Schematic illustration of

pouch type Si full cell under the application of high external stack pressure
(800 kPa) **f** Cycling performance of Si full cell containing HM separator under the
externally applied stack pressure of 800 kPa. **g** Comparison of the cell perfor-
mances between this work and previously reported full cells with micro-sized Si
anodes in terms of four parameters: cycle number of Si full cells (*x*-axis), areal
capacity (*y*-axis), capacity retention (heatmap), and charge current density (dia-
meter). The number assigned to each circle corresponds to the serial number in
Supplementary Table 5 (refs. 9,13,26–38).

compared to the result obtained at a stack pressure of 100 kPa (Fig. 5f
and Supplementary Fig. 32), demonstrating the effectiveness of the
higher stack pressure of 800 kPa. In contrast, the full cell with the PE
separator suffered from rapid capacity degradation, which was more
severe than that shown in Fig. 1a. This poor cycling performance of the
PE separator can be attributed to the accelerated pore collapse at the
elevated stack pressure of 800 kPa. It should be noted that this cycling
performance of the HM separator significantly exceeds those of pre-
viously reported full cells with micro-sized Si anodes (Fig. 5g and
Supplementary Table 5), particularly in terms of the areal capacity and
charge/discharge current rate, underscoring the electrochemical

viability of the HM separator in extending the cycle life of practical Si
full cells.

Discussion
In summary, we demonstrated that the deformation of battery
separator pores, alongside the well-known issue of Si pulverization, has
a critical impact on the cycling performance of Si anodes. Particularly,
the mechano-structural characterization of Si full cells revealed the
disruption of the pores of PE separators during cycling owing to the
local compressive stress generated by the volume expansion of Si.
Upon exposure to internal stress exceeding 6 MPa in Si full cells, the

porous structure of the PE separator collapsed, a phenomenon referred to as mechanical shutdown, ultimately blocking the ion transport. This mechanical shutdown behavior was quantitatively elucidated through SECM analysis as a function of cycle number and discussed in relation to the cycling degradation of the Si anode. Based on the electromechanical understanding of separators, we designed the HM separator (>1 GPa) capable of maintaining its porous structure even when paired with Si anode during cycling. Driven by this mechanical resistance, a high-areal-capacity pouch-type Si full cell with the HM separator achieved a stable cyclability (capacity retention = 88% after 400 cycles) at a fast charge rate of 4.5 mA cm^{-2}, outperforming those of previously reported Si full cells. This study demonstrated the importance of cell-based approaches in enabling the long-cyclable Si full cells. Particularly, it highlights the importance of the mechanical shutdown phenomena of separators in Si full cells plagued with high internal stress.

Methods

Design and fabrication of the HM separator

The high modulus (HM) separator was fabricated using a concurrent electrospraying (for Al_2O_3)/electrospinning (for polyacrylonitrile (PAN)) technique, followed by roll pressing. Briefly, Al_2O_3 (provided by LG Energy Solution) was dispersed in a solvent mixture of acetone/butanol (7/3 (v/v)), and the PAN (concentration = 9 wt%, Aldrich) solution was prepared by dissolving PAN (molecular weight = 150,000 g mol^{-1}) in dimethylformamide (DMF) at 70 °C for 12 h. The Al_2O_3 suspension and PAN solution were individually subjected to electrospraying and electrospinning processes concurrently through two different nozzles at room temperature. The processing conditions were as follows: an applied voltage of 12 kV with a feed rate of 3.5 μL min^{-1} (for the electrospinning) and 18 kV with a feed rate of 80 μL min^{-1} (for the electrospraying). The self-standing and flexible HM separator (thickness ~ 30 μm) was obtained after subjecting the separator to a roll pressing process.

Structural and physicochemical characterization of the separators

The surface and cross-sectional morphologies of the separators were characterized using a field emission scanning electron microscope (FE-SEM) (S-4800, Hitachi) combined with an energy-dispersive X-ray spectrometer (EDS) (JSM 6400, JEOL). The porosity and pore size distribution of the separators were analyzed using a Hg porosimeter (Auto pore IV 9520, Micromeritics), and the mechanical properties of the separators were measured using nanoindentation (Nanoindenter by KLA-Tencor). The thermogravimetric analysis (TGA) analysis (SDT Q600, TA Instruments) was performed at a heating rate of 10 °C min^{-1} under an air atmosphere to estimate the composition ratio of the HM separator.

Internal force measurement during lithiation/delithiation of Si

The experimental setup for the operando measurement of the internal force evolution in the Si full cells during repeated lithiation/delithiation is depicted in Supplementary Fig. 6. The internal force newly generated within the pouch-type cells was measured using the subminiature load cells (LC307, Omega Engineering) connected to strain gauge panel meters (DP25B-S, Omega Engineering). The measurements were conducted after one formation cycle at a charge/discharge current rate of 0.1 C, followed by a degassing step.

SECM analysis of the separators

The scanning electrochemical microscopy (SECM) measurements were conducted using a scanning probe workstation (M470, Biologic). An Au electrode (substrate, diameter of 10 mm) embedded in epoxy resin (Biologic) and a Pt microprobe (tip, diameter of 1 μm) (U-P5/1, Biologic) were used as the working electrodes. The Au electrode was polished using 0.05 μm alumina micro-polishing cloth and cleaned with water. Pristine or cycled separators were placed on the Au electrode during the analysis. A non-aqueous Ag/Ag$^+$ reference electrode was used, consisting of an Ag wire immersed in a solution of 0.1 M tetrabutylammonium perchlorate (TBAP) in dimethyl sulfoxide (DMSO) containing 0.01 M silver nitrate (AgNO$_3$). A Pt mesh was utilized as an auxiliary electrode. A liquid electrolyte consisting of 2 mM of ferrocene (Fc) redox mediator dissolved in 0.1 M TBAP in DMSO was used for the analysis.

Electrochemical characterization of the separators and Si full cells

The ionic conductivity of the separators was estimated by electrochemical impedance spectroscopy (EIS) analysis using blocking cells (SUS|separator|SUS) in 2032-type coin cells, with an applied amplitude of 14.1 mV, which corresponds to the V$_{rms}$ of 10 mV over the frequency range from 10^{-2} to 10^6 Hz, using a potentiostat/galvanostat (VSP classic, Bio-Logic) at room temperature (25 °C). To measure the ionic conductivity of the cycled polyethylene (PE) and HM separators, the cycled cells were disassembled, and the cycled separators were collected at specific cycle numbers (100th, 200th, and 400th cycle). The pouch-type full cells were composed of LiNi$_{1-x-y-z}$Co$_x$Mn$_y$Al$_z$O$_2$ (NCMA) cathode (areal capacity of 4.5 mAh cm^{-2}), Si anode (areal capacity of 8.5 mAh cm^{-2}) or graphite anode (areal capacity of 5.0 mAh cm^{-2}), and liquid electrolyte (1 M LiPF$_6$ in ethyl methyl carbonate (EMC)/fluoroethyl carbonate (FEC) = 7/3 (v/v)). All electrodes examined herein were supplied by LG energy solution. To fabricate the pouch-type full cells, the NCMA cathode, graphite anode, and Si anode were cut into 20 mm × 20 mm and 30 mm × 30 mm pieces, respectively. The Al and Ni tabs were welded onto the NCMA cathode, graphite anode, and Si anode, respectively, using a welding machine (KM-40ST, Kormax system). The electrodes and separator were stacked and sealed with a pouch film, followed by injection of liquid electrolyte (~ 5 g Ah^{-1}). The cell fabrication was performed in a dry room, where the dew point is controlled below −40 °C. The electrochemical performance of the pouch-type full cells was evaluated under a fixed pressure of 100 kPa, in which the cell was cycled at a charge/discharge current density of 1.0 C (4.5 mA cm^{-2})/0.5 C (2.25 mA cm^{-2}) for Si anode and 0.33 C (1.5 mA cm^{-2})/0.33 C (1.5 mA cm^{-2}) for graphite anode and voltage range of 3.2 – 4.25 V. The charge/discharge performance of the cells was investigated using a cycle tester (PNE Solution) at room temperature (25 °C).

Construction of the 3D digital-twin structures of Si full cells

Separator structure: The structural information of the PE and HM separators, including the fiber thickness, orientation, and particle size, was gathered from their SEM images using ImageJ and OrientationJ software (Supplementary Fig. 9). Using these parameters, virtual 3D separator structures were constructed in GeoDict 2023 (Math2Market, Germany), reflecting the design of PE separator (thickness ~ 20 μm and porosity ~ 47%, Asahi Co.) and HM separator (thickness ~ 30 μm and porosity ~ 52%). The PE and PAN fibers were generated using the PaperGeo module, and Al_2O_3 particles were drawn using GrainGeo in the 10 μm × 10 μm × (separator thickness) μm domain with 0.050 μm voxel length. Additionally, the randomness of the fiber straightness in the PE separator was controlled by comparing it to the SEM images.

Electrode structure: 3D electrode structures for the NCMA and pure micro-sized Si were designed with different electrode compositions ((NCMA:carbon black:PVdF = 90:5.5:4.5, wt%) and (Si:Super-P:PAA = 80:10:10, wt%)) under different structural conditions (NCMA electrode: 8.90 mg cm^{-2}, 30.7 μm; pure Si electrode: 0.88 mg cm^{-2}, 9.8 μm)[13,25]. The electrode active particles (spherical NCMA and polyhedron-type Si) and CBD (carbon and binder domain) were formed using the "Create Grain" and "Add binder" functions in the GrainGeo module, respectively. The domain size of the electrode

structures was set as 10 μm × 10 μm × (electrode thickness) μm. To estimate the contact area, it was extended to 20 μm × 20 μm × (electrode thickness) μm.

Mechanical/structural analysis of the separator and electrode structures through digital-twin simulation

The digital-twin separator and pure micro-sized Si anode structures were attached in the LayerGeo module and compressed at a strain rate of – 20% using the ElastoDict module. Considering the mechanical properties and elastic-plastic deformation of materials, the applied z-directional stresses on the digital-twin structures were calculated during the mechanical compression. The ionic conductivity of both the pristine and deformed structures was estimated under a potential difference of 1 V in the ConductoDict module. The surface-to-surface contact area of the NCMA cathode–separator–Si anode was quantified using the functions of the LayerGeo module and MatDict module.

Data availability

All relevant data generated in this study are provided in the main figure, supplementary information and Source data. The data that support the findings of this study are available from the corresponding author upon request. Source data are provided in this paper.

References

1. Tarascon, J. M. & Armand, M. Issues and challenges facing rechargeable lithium batteries. *Nature* **414**, 359–367 (2001).
2. Zhang, X., Wang, D. & Qiu, X. Stable high-capacity and high-rate silicon-based lithium battery anodes upon two-dimensional covalent encapsulation. *Nat. Commun.* **11**, 3826 (2020).
3. Kim, N., Kim, Y., Sung, J. & Cho, J. Issues impeding the commercialization of laboratory innovations for energy-dense Si-containing lithium-ion batteries. *Nat. Energy* **8**, 921–933 (2023).
4. Tan, D. H. S., Chen, Y. T. & Meng, Y. S. Carbon-free high-loading silicon anodes enabled by sulfide solid electrolytes. *Science* **373**, 1494–1499 (2021).
5. Wang, Q. et al. High-performance microsized Si anodes for lithium-ion batteries: insights into the polymer configuration conversion mechanism. *Adv. Mater.* **34**, 2109658 (2022).
6. Zhu, G., Chao, D., Xu, W., Wu, M. & Zhang, H. Microscale silicon-based anodes: fundamental understanding and industrial prospects for practical high-energy lithium-ion batteries. *ACS Nano* **15**, 15567–15593 (2021).
7. Liu, N., Lu, Z. & Zhao, J. A pomegranate-inspired nanoscale design for large-volume-change lithium battery anodes. *Nat. Nanotechnol.* **9**, 187–192 (2014).
8. Zhang, X., Guo, R., Li, X. & Zhi, L. Scallop-inspired shell engineering of microparticles for stable and high volumetric capacity battery anodes. *Small* **14**, e1800752 (2018).
9. Li, Y., Yan, K. & Lee, H. W. Growth of conformal graphene cages on micrometre-sized silicon particles as stable battery anodes. *Nat. Energy* **1**, 15029 (2016).
10. Zhu, G. et al. Boron doping-induced interconnected assembly approach for mesoporous silicon oxycarbide architecture. *Natl. Sci. Rev.* **8**, nwaa152 (2020).
11. Cao, Z., Zheng, X., Qu, Q., Huang, Y. & Zheng, H. Electrolyte design enabling a high-safety and high-performance Si anode with a tailored electrode–electrolyte interphase. *Adv. Mater.* **33**, 2103178 (2021).
12. Yang, G. et al. Robust solid/electrolyte interphase (SEI) formation on Si anodes using glyme-based electrolytes. *ACS Energy Lett.* **6**, 1684–1693 (2021).
13. Choi, S., Kwon, T.-W., Coskun, A. & Choi, J. W. Highly elastic binders integrating polyrotaxanes for silicon microparticle anodes in lithium ion batteries. *Science* **357**, 279–283 (2017).
14. Lopez, J. et al. The effects of cross-linking in a supramolecular binder on cycle life in silicon microparticle anodes. *ACS Appl. Mater. Interfaces* **8**, 2318–2324 (2016).
15. Zhang, S. et al. An elastic cross-linked binder for silicon anodes in lithium-ion batteries with a high mass loading. *ACS Appl. Mater. Interfaces* **15**, 6594–6602 (2023).
16. Shang, T., Wen, Y., Xiao, D., Gu, L. & Li, H. Atomic-scale monitoring of electrode materials in lithium-ion batteries using in situ transmission electron microscopy. *Adv. Energy Mater.* **7**, 1700709 (2017).
17. Narayanan, S., Ulissi, U. & Gibson, J. S. Effect of current density on the solid electrolyte interphase formation at the lithium|Li6PS5Cl interface. *Nat. Commun.* **13**, 7237 (2022).
18. Choi, W., Shin, H.-C., Kim, J. M., Choi, J.-Y. & Yoon, W.-S. Modeling and applications of electrochemical impedance spectroscopy (EIS) for lithium-ion batteries. *J. Electrochem. Sci. Technol.* **11**, 1–13 (2020).
19. Wang, S. Electrochemical impedance spectroscopy. *Nat. Rev. Methods Prim.* **1**, 41 (2021).
20. Shen, M., Ishimatsu, R., Kim, J. & Amemiya, S. Quantitative imaging of ion transport through single nanopores by high-resolution scanning electrochemical microscopy. *J. Am. Chem. Soc.* **134**, 9856–9859 (2012).
21. Lagadec, M. F., Zahn, R., Müller, S. & Wood, V. Topological and network analysis of lithium ion battery components: the importance of pore space connectivity for cell operation. *Energy Environ. Sci.* **11**, 3194–3200 (2018).
22. Kováčik, J. Correlation between Young's modulus and porosity in porous materials. *J. Mater. Sci. Lett.* **18**, 1007–1010 (1999).
23. Cannarella, J. & Arnold, C. B. The effects of defects on localized plating in lithium-ion batteries. *J. Electrochem. Soc.* **162**, A1365 (2015).
24. Mussa, A. S., Klett, M., Lindbergh, G. & Lindström, R. W. Effects of external pressure on the performance and ageing of single-layer lithium-ion pouch cells. *J. Power Sources* **385**, 18–26 (2018).
25. Kim, U.-H., Kuo, L.-Y., Kaghazchi, P., Yoon, C. S. & Sun, Y.-K. Quaternary layered Ni-rich NCMA cathode for lithium-ion batteries. *ACS Energy Lett.* **4**, 576–582 (2019).
26. Li, A. M., Wang, Z. & Pollard, T. P. High voltage electrolytes for lithium-ion batteries with micro-sized silicon anodes. *Nat. Commun.* **15**, 1206 (2024).
27. Li, Q. et al. F. Wang. Interphasial pre-lithiation and reinforcement of micro-Si anode through fluorine-free electrolytes. *Angew. Chem. Int. Ed.* **62**, e202310297 (2023).
28. Xu, Z. et al. Silicon microparticle anodes with self-healing multiple network binder. *Joule* **2**, 950–961 (2018).
29. Kang, M. S. et al. High-areal-capacity of micron-sized silicon anodes in lithium-ion batteries by using wrinkled-multilayered-graphenes. *Energy Storage Mater.* **50**, 234–242 (2022).
30. Zhang, W., Liu, S. & Wang, C. Bi-layer carbon design for microparticulate silicon anodes. *Natl. Sci. Rev.* **8**, nwab057 (2021).
31. Zhang, Y. et al. Z. Chen. Diatomite-derived hierarchical porous crystalline-amorphous network for high-performance and sustainable Si anodes. *Adv. Funct. Mater.* **30**, 2005956 (2020).
32. An, W., Gao, B. & Mei, S. Scalable synthesis of ant-nest-like bulk porous silicon for high-performance lithium-ion battery anodes. *Nat. Commun.* **10**, 1447 (2019).
33. Li, X. P. et al. Design of porous Si/C–graphite electrodes with long cycle stability and controlled swelling. *Energy Environ. Sci.* **10**, 1427–1434 (2017).
34. Son, Y. et al. Calendering-compatible macroporous architecture for silicon–graphite composite toward high-energy lithium-ion batteries. *Adv. Mater.* **32**, 2003286 (2020).
35. Ko, M., Chae, S. & Ma, J. Scalable synthesis of silicon-nanolayer-embedded graphite for high-energy lithium-ion batteries. *Nat. Energy* **1**, 16113 (2016).

36. Wu, Y., Liu, X., Wang, L., Amine, K. & Ouyang, M. Development of cathode-electrolyte-interphase for safer lithium batteries. *Energy Storage Mater.* **37**, 77–86 (2021).

37. Xiao, Z. TiO$_2$ as a multifunction coating layer to enhance the electrochemical performance of SiOx@TiO$_2$@C composite as anode material. *Nano Energy* **77**, 105082 (2020).

38. Chen, F., Han, J., Kong, D. & Yuan, Y. 1000 Wh L^{-1} lithium-ion batteries enabled by crosslink-shrunk tough carbon encapsulated silicon microparticle anodes. *Natl. Sci. Rev.* **8**, nwab012 (2021).

Acknowledgements

Author contributions

J.Y.Seo and S.Y.L. designed this work. J.Y.Seo performed the experimental characterization and electrochemical tests. S.H.K. performed the theoretical calculations. J.H.K. conducted the LEIS analysis. Y.H.L, J.Y.Shin, S.J., and D.W.S. provided material sources. Y.M.L. and S.Y.L. supervised the overall project. All authors contributed to finalizing the manuscript.

Competing interests

The authors declare no competing interests.

Additional information

Supplementary information The online version contains supplementary material available at https://doi.org/10.1038/s41467-024-54313-y.

Correspondence and requests for materials should be addressed to Yong Min Lee or Sang-Young Lee.

Peer review information *Nature Communications* thanks Changmin Shi, Yongming Sun, and the other anonymous reviewer(s) for their contribution to the peer review of this work. A peer review file is available.

Reprints and permissions information is available at http://www.nature.com/reprints

Publisher's note Springer Nature remains neutral with regard to jurisdictional claims in published maps and institutional affiliations.